Title

Acoustic Resonance Tuning by High-Order Lorentzian Mixing.

Journal

Nano Letters, 24(24)

Authors

Kim, Hyeongpin

Seong, Yeolheon

Kwon, Kiwon

et al.

Publication Date

2024-05-13

DOI

10.1021/acs.nanolett.4c00335

Peer reviewed

NANO LETTERS

pubs.acs.org/NanoLett
Letter

Acoustic Resonance Tuning by High-Order Lorentzian Mixing

Hyeongpin Kim, Yeolheon Seong, Kiwon Kwon, Taek Yong Hwang, and Heedeuk Shin*

Cite This: *Nano Lett.* 2024, 24, 7143–7149
Read Online

ACCESS | Metrics & More | Article Recommendations | Supporting Information

ABSTRACT: Nanoscale mechanical resonators have attracted a great deal of attention for signal processing, sensors, and quantum applications. Recent progress in ultrahigh-Q acoustic cavities in nanostructures allows strong interactions with various physical systems and advanced functional devices. Those acoustic cavities are highly sensitive to external perturbations, and it is hard to control those resonance properties since those responses are determined by the geometry and material. In this paper, we demonstrate a novel acoustic resonance tuning method by mixing high-order Lorentzian responses in an optomechanical system. Using weakly coupled phononic-crystal acoustic cavities, we achieve coherent mixing of second- and third-order Lorentzian responses, which is capable of the fine-tunability of the bandwidth and peak frequency of the resonance with a tuning range comparable to the acoustic dissipation rate of the device. This novel resonance tuning method can be widely applied to Lorentzian-response systems and optomechanics, especially active compensation for environmental fluctuation and fabrication errors.

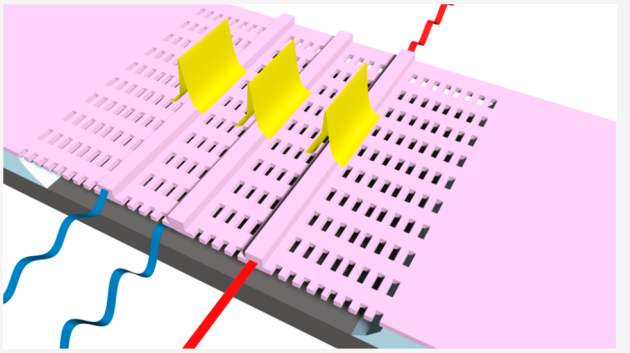

KEYWORDS: *photonic integrated circuits, silicon photonics, acousto-optic effects, on-chip Brillouin scattering, optomechanics*

Advances in high-quality mechanical oscillators in nanostructures enable strong interaction between mechanical oscillators and various physical systems.[1−4] Using the universal interactions, mechanical oscillators play important roles in various applications such as sensors,[5−12] RF and optical signal processing,[13−26] and quantum transduction.[27−31] While high-Q acoustic cavities show interesting applications, one of the main challenges in implementing such systems is the sensitivity of the resonant frequency to environmental conditions and fabrication errors. Given that high-Q acoustic resonators have a highly narrow bandwidth, such deviations can result in out-of-band operation. Active control of mechanical oscillators, for instance, the peak frequency and bandwidth, can be a solution to compensate for such errors. In addition, peak frequency shifting can enhance operation ranges. Bandwidth is related to the quality factor, and controlling it switches between high signal-to-noise ratio and high-speed operations.

To change the properties of mechanical oscillators, changes in physical parameters such as stiffness, surface stress, and dimensions are required but challenging since those are fixed at a choice of materials and geometries, so postlithographic trimmings are typically required.[32,33] On the other hand, there are some strategies to allow active control such as stiffness,[34,35] surface stress,[36] thermal effects,[37,38] and acoustic nonlinear effects.[39,40] Such mechanical parameter modulations can be demonstrated using piezoelectric materials. Also, recently low-dimensional materials show great tunability.[41] However, these methods limit the choice of materials such as piezoelectric and 2D materials, so those are not suitable for wide applications.

In this paper, we present the first demonstration of acoustic resonance tuning by mixing high-order Lorentzian responses by using forward stimulated Brillouin scattering in telecom-band lasers and GHz acoustic modes. We fabricated three coupled phononic crystal acoustic cavities that are colocated with three optical waveguides and weakly coupled to each other to avoid mode splitting. The device coherently mixes second- and third-order Lorentzian responses and shows discrete bandwidth tuning and continuous peak frequency tuning comparable to the dissipation rate of acoustic cavities. In addition, we generalize our concept to higher-order Lorentzian functions, and this significantly enhances the tuning range. Notably, our method of high-order Lorentzian responses enables the active tuning of mechanical resonators without changes in mechanical properties. We demonstrate our idea in the Brillouin optomechanical system, but it can be generalized to various applications of mechanical oscillators, especially active compensation of environmental fluctuation, laser heating, and fabrication errors.

Received: January 22, 2024
Revised: April 19, 2024
Accepted: April 24, 2024
Published: May 13, 2024

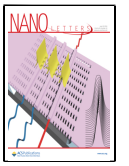

https://doi.org/10.1021/acs.nanolett.4c00335
Nano Lett. 2024, 24, 7143−7149

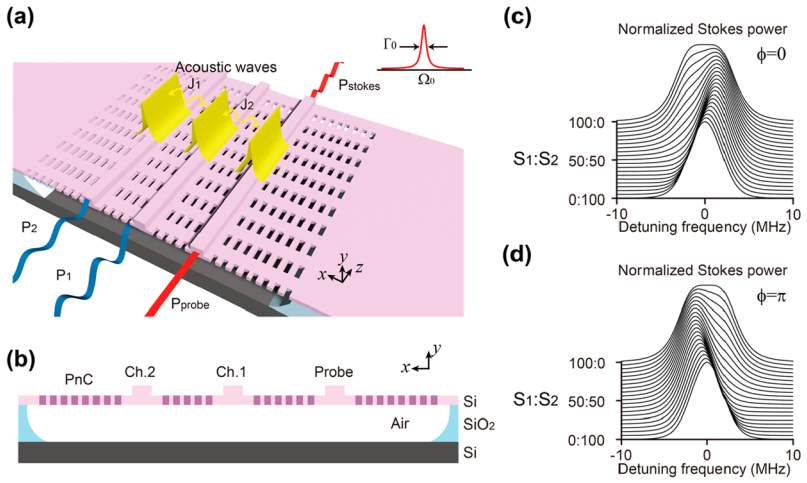

Figure 1. Acoustic resonance tuning by mixing of second- and third-order Lorentzian responses. (a) Schematic illustration of an optically tunable acoustic resonance on a silicon-on-insulator chip. Here, telecom-band lasers and GHz acoustic modes are used. The device consists of three acoustic cavities defined by phononic crystalline defects that confine transverse acoustic waves (yellow surfaces) and three optical waveguides colocated with the acoustic cavities. The acoustic cavities are weakly coupled through phononic crystals with coupling strengths of J_1 and J_2. Oscillating pumps (represented by blue lines) are injected into channels 1 and 2 with a relative phase between them, ϕ, and a continuous-wave laser (represented by red lines) on the probe channel is scattered by the acoustic waves. The Stokes signal of the scattered probe has a Lorentzian-shaped spectrum with a peak frequency Ω_0 and a bandwidth Γ_0. (b) The cross-section of the demonstrated device. Three rib-type optical waveguides correspond to Probe, Ch.1, and Ch.2. Phononic crystals are fabricated beside optical waveguides to define acoustic cavities. The top silicon membrane is floating to prevent acoustic leakage through the buried oxide layer. (c, d) Simulation results of the normalized Stokes output spectra. The ratio of balanced input powers S_1 and S_2 is varied, and the relative phase is set in (c) $\phi = 0$ and (d) $\phi = \pi$, respectively.

Figure 1a,b displays the schematics of our optically tunable acoustic resonance device. The device consists of a phononic crystal (PnC) membrane that incorporates three rib-type optical waveguides embedded at the center of the PnC line defects. Oscillating pump light signals P_1 and P_2 are injected into channels 1 and 2, while continuous-wave laser light is introduced into the probe channel. The frequency of the oscillating pump is adjusted to match the compressive acoustic resonant frequency of the PnC line defects, thereby confining the transverse acoustic waves (illustrated on yellow surfaces). The three acoustic cavities, weakly coupled through the acoustic leakage in the PnC structure with coupling strengths denoted as J_1 and J_2, allow the acoustic fields excited in channels 1 and 2 to couple with the probe channel. Subsequently, the continuous-wave laser in the probe channel experiences scattering due to photoelastic effects, generating new frequency components. The spectrum of the Stokes field, being the frequency-downshifted scattered component, exhibits a Lorentzian shape with the center frequency Ω_0 of the acoustic resonant frequency and the bandwidth Γ_0, the dissipation rate of the acoustic wave.

Here we demonstrate adjusting of the acoustic bandwidth and peak frequency. In this system, the acoustic field in the probe channel is approximately described by

$$|B_{pr}|^2 \approx |\chi_2 S_1 + \chi_3 S_2 e^{i\phi}|^2 \quad (1)$$

where χ_2 and χ_3 are the second- and third-order Lorentzian responses defined by $\{[(\Delta\Omega - J)^2 + (\Gamma_0/2)^2][(\Delta\Omega + J)^2 + (\Gamma_0/2)^2]\}^{-1}$ and $\{[(\Delta\Omega - J)^2 + (\Gamma_0/2)^2][(\Delta\Omega)^2 + (\Gamma_0/2)^2][(\Delta\Omega + J)^2 + (\Gamma_0/2)^2]\}^{-1}$, respectively. $\Delta\Omega$ is the detuning from the acoustic resonant frequency. J in eq 1 is defined as $J = (J_1^2 + J_2^2)^{1/2}$. ϕ is the relative phase between the two pump lights. We define the balanced input powers as $S_1 = \Gamma_0/2 \times P_1$ and $S_2 = J \times P_2$. Since the acoustic modes excited from channels 1 and 2 have unequal energy distributions on the probe channel, we define the balanced powers to make the distribution equal and the analysis easy.

In this paper, we limit our study to a weakly coupled regime, $J \leq \Gamma_0/2$, to avoid peak splitting. When two modes are hybridized, the avoided mode crossing is proportional to the coupling strength, but if the spectra of modes are broad, we cannot distinguish the modes. Mathematically, the peak positions can be found by the zeros of the derivative of the response functions, which means the points where the slopes are zero. This inequality satisfies the solutions of the derivative are imaginary numbers, then peak splitting is avoided. $\Gamma_0/2$ is an upper bound of the coupling J. In silicon forward Brillouin scattering, it has a value of several MHz,[16−18,42,43] but the same rule can be applied to other mechanical systems. The detailed theoretical analysis is presented in the Supporting Information.

The proposed acoustic-resonance tunable device, featuring three coupled acoustic cavities, enables the tuning of bandwidth and peak frequency by varying the optical power ratio between the input pump channels. When only channel 1 is excited, eq 1 shows a wide second-order response of χ_2. In contrast, when only channel 2 is excited, the system exhibits a narrow third-order response of χ_3. These two different Lorentzian responses have different bandwidths. The peak frequency can be tuned by coherently mixing the second- and third-order responses. By modification of the mixing ratio and the relative phase between input pumps, the center frequency can be continuously altered.

We calculate the resonant response to observe its bandwidth and peak frequency tuning capabilities. Figure 1c,d shows the calculated results of the normalized Stokes output in three coupled acoustic cavities with different relative phases of $\phi = 0$ and π, respectively. The two acoustic-wave cavities have identical resonant frequencies, dissipation rates, and Brillouin gain coefficients. We designed the phonon dissipation rate Γ_0 to be equal to twice the coupling strength J, $\Gamma_0 = 2J = 5$ MHz, to prevent mode splitting and maximize the tuning ranges for

https://doi.org/10.1021/acs.nanolett.4c00335
Nano Lett. 2024, 24, 7143−7149

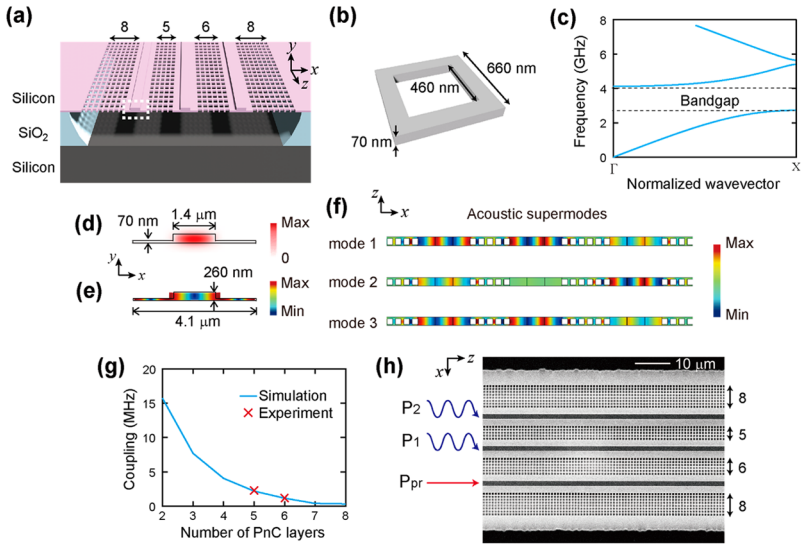

Figure 2. Device design. (a) Cross-sectional view of the optically tunable on-chip acoustic-resonance device showcasing the three optical waveguides, three line defects, and phononic crystals fabricated on the top silicon layer with the buried oxide layer being wet-etched. The numbers of PnC layers at the end sides, between channels 1 and 2, and between channel 1 and the probe channel are 8, 5, and 6, respectively. (b) The geometry of the square-shaped phononic crystal unit cell. (c) Dispersion curves of the phononic crystals, showing the bandgap in the range of 2.73−4.12 GHz. (d) Electric field of the fundamental TE mode, (e) Acoustic displacement of the 3.1 GHz compressive acoustic mode on a waveguide, with its cross-section indicated by the white dotted box in (a). (f) Three acoustic supermodes across the three coupled acoustic cavities, with Modes 1−3 corresponding to the modes at $\Omega_0 - J$, Ω_0, and $\Omega_0 + J$, respectively. (g) Variation of coupling strength between two cavities as a function of the number of PnC layers. The experimental data points are extracted from the data fitting based on results shown in Figures 3 and 4. (h) Top-down view from a scanning electron microscope of the fabricated sample, showing oscillating optical pumps 2 and 1 injected into channels 2 and 1, respectively, and the continuous-wave probe injected into the probe channel.

both bandwidth and peak frequency. We set the sum of S_1 and S_2 as constant and calculate the normalized Stokes output while varying the power ratio between S_1 and S_2. The bandwidth of the acoustic resonance can be adjusted by exciting second- and third-order responses, having bandwidths of $\sqrt{2}\,\Gamma_0$ and $0.867\Gamma_0$, respectively. Moreover, compared to the single-pole Lorentzian response with a bandwidth Γ_0, the third-order response enables a 13% improvement in narrow-band operation, even with the same dissipation rate.

The device can adjust the peak frequency by coherent mixing of two Lorentzian responses, χ_2 and χ_3. Figure 1c,d shows continuous tuning of the peak frequency with the maximum shifting $\pm 0.27\Gamma_0$ when S_1:S_2 = 70:30. Considering that the dissipation rate of acoustic waves in forward Brillouin scattering typically spans several MHz, our device is able to modify its bandwidth and peak frequency within a similar range. Further details of the theoretical models are provided in the Supporting Information.

The design of the optically acoustic-resonance tunable device is shown in Figure 2. Figure 2a illustrates the schematic cross-sectional view of three rib-type optical waveguides situated on a floating membrane with PnC structures. The phononic crystals, positioned beside the waveguides, consist of a square lattice of square-shaped holes, as shown in Figure 2b. Their period, hole size, and thickness are 660, 460, and 70 nm, respectively. Figure 2c presents the PnC dispersion curve displaying a bandgap in the range of 2.73−4.12 GHz, which effectively confines the transverse acoustic modes within the line defect range. The detailed analysis of phononic crystals and acoustic modes is displayed in the Supporting Information.

Figure 2d,e illustrates the optical field and acoustic displacement in the cross-section of the waveguide (indicated by the white dotted box in Figure 2a). We utilize the fundamental TE mode, as shown in Figure 2d, and a 3.1 GHz compressive acoustic mode, which has repeatedly compressed and expanded displacement over the cross-section of the waveguide, as shown in Figure 2e. The three optical waveguides are identical, with a thickness of 260 nm, a width of 1.4 μm, and an etching depth of 190 nm. The three PnC line defects, each with a width of 4.1 μm for the acoustic-mode wing, as seen in Figure 2e, confine the 3.1 GHz compressive acoustic modes, serving as acoustic cavities. These cavities are weakly coupled via phononic crystals, resulting in three acoustic supermodes, as shown in Figure 2f. However, the three acoustic supermodes overlap because the coupling strength J is equal to or smaller than the dissipation rate $\Gamma_0/2$, so we cannot observe the mode splitting.

The coupling strength between two acoustic cavities can be controlled by varying the number of PnC layers, as shown in Figure 2g. With an increase in the number of PnC layers, the coupling strength decreases discretely. To minimize acoustic leakage at the end sides, we have employed 8 layers of phononic crystals, as shown in Figure 2h. The couplings between the three acoustic cavities are asymmetric, featuring 5 PnC layers between channels 2 and 1, and 6 PnC layers between channel 1 and the probe channel, resulting in corresponding coupling strengths of 2.3 and 1.2 MHz, respectively. This asymmetric coupling design aims to fulfill two conditions: $\Gamma_0/2 = J = (J_1^2 + J_2^2)^{1/2}$ and control of the split ratio between S_1 and S_2. The first condition ensures the avoidance of mode splitting and maximizes the tunability. For simpler optical power control, we set $\Gamma_0/2 \approx J_1 \gg J_2$, which simplifies the balanced split ratio to become S_1:S_2 = P_1:P_2. However, because J_2 is directly proportional to the Stokes signal on the probe channel, a small J_2 results in low efficiency of acoustic-wave probing. Therefore, we designed asymmetric

https://doi.org/10.1021/acs.nanolett.4c00335
Nano Lett. 2024, 24, 7143−7149

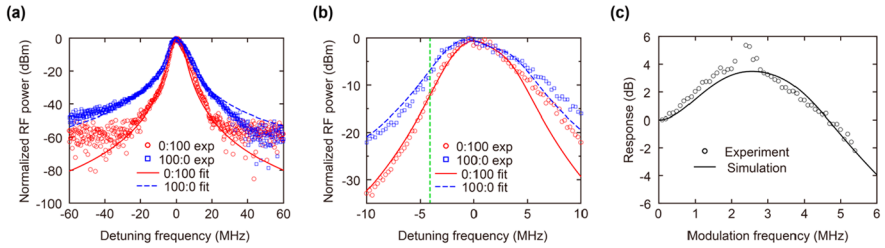

Figure 3. Bandwidth tunability and tuning speed. (a) Experimental output Stokes spectra for wide (S_1:S_2 = 100:0) and narrow (S_1:S_2 = 0:100) resonances. Red (blue) circle (square) markers and solid (dashed) lines are experimental data and fitted curves for the narrow (wide) Lorentzian responses. (b) Magnified view of the spectra near the peak. The vertical green dashed line indicates the detuning frequency of −4.1 MHz. (c) Measurement of bandwidth tuning speed against the modulation frequency at a detuning frequency of −4.1 MHz. The graph includes a curve from a numerical simulation of coupled acoustic cavities for comparison.

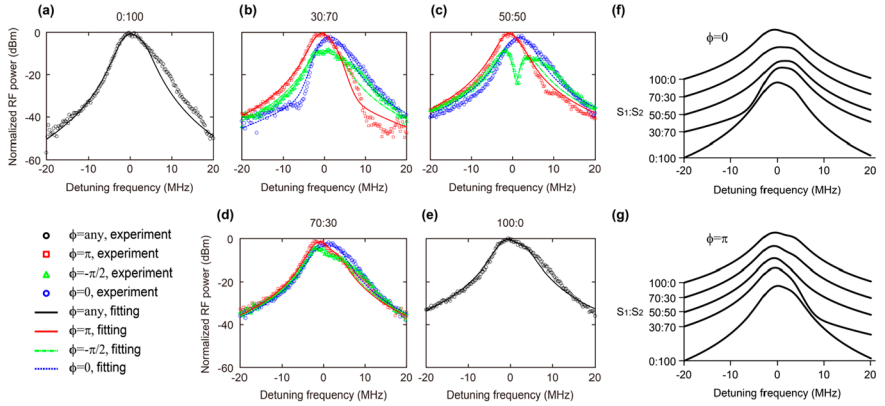

Figure 4. Frequency tunability in our system. The output Stokes spectra for various pump power ratios between S_1 and S_2 are presented: (a) 0:100, (b) 30:70, (c) 50:50, (d) 70:30, and (e) 100:0. The spectra are measured at relative phases of 0, π, and $-\pi/2$ between the two pumps. The markers and curves represent the experimental data and fitting results, respectively. Red square markers and solid lines are for $\phi = \pi$, green triangle markers and dash-dotted lines for $\phi = -\pi/2$, and blue circle markers and dotted lines for $\phi = 0$. In (a) and (e), black circle markers and solid lines indicate scenarios where the pump is inserted into the single pump channel, rendering the relative phase irrelevant. (f,g) Collections of fitting curves from (a−e) for relative phases of 0 and π, respectively.

couplings of J_1 and J_2. The coupling strength simulation is described in the Supporting Information.

The photonic waveguides in our design have a total length of about 1.2 cm and are floated over a span of 5 mm. They exhibit propagation losses of about 0.7 dB/cm, and the grating coupler efficiencies for fiber-to-chip coupling are around 54% per facet. We determined the acoustic properties of our sample by fitting the experimental results. The Brillouin gain coefficients, dissipation rates, and coupling coefficients were extracted by fitting the experimental data to a model based on eq S13 in the Supporting Information. The resulting Brillouin gain coefficients are [510, 580, 310] W^{-1} m^{-1}, and the dissipation rates are [5.4, 4.7, 5.3] MHz, respectively, with an average dissipation rate of 5.13 MHz. The coupling strengths J_1 and J_2 are [2.3, 1.2] MHz, respectively (displayed in Figure 2h). The target acoustic resonant frequency was set at 3.135 GHz for 4.1 μm line defects, but fabrication errors caused the resonant frequency deviations of channels 2, 1, and the probe, measured as [−0.98, −0.74, 0.15] MHz, respectively. These nonidentical values result in the asymmetric peak shape observed in Figure 3b. The detail of the experimental setup is described in the Supporting Information.

First, we examined the bandwidth tunability of the device. Figure 3a shows second- and third-order response spectra when the input pump is injected into channel 1 or 2, while Figure 3b provides a magnified view near the peak. When the pump is excited only in channel 1, the spectrum follows a second-order response, χ_2, but when it is excited in channel 2, it adheres to a third-order response, χ_3. The fitting curves, based on the model of the corresponding response functions, are well-matched with the experimental data. When channel 1 or 2 is excited, the 3 dB bandwidths are 5.75 and 4 MHz, respectively, resulting in a bandwidth that is 1.43 times wider compared to χ_3.

Next, we assessed the bandwidth-tuning speed of our device by observing the RF power of the output Stokes light in the time domain. We utilize the zero-span feature of a spectrum analyzer with an 8-MHz resolution and video bandwidth for this purpose.[18] As seen in Figure 3b, the RF powers of Stokes light for narrow bandwidth operations S_1:S_2 = 100:0 and wide operations S_1:S_2 = 0:100 are similar at the peak resonant frequency but exhibit a contrast of 4.7 dB at −4.1 MHz of the detuning frequency from the center, as seen in Figure 3b.

To estimate the bandwidth-tuning speed limit, we insert a −4.1 MHz detuned oscillating pump and measure the RF power of the output Stokes light in the time domain while rapidly switching the input pump ports fast sinusoidally using a variable beam splitter. Due to the bandwidth limitation of the spectrum analyzer in the experimental setup, the modulation frequencies were observable only up to 5.3 MHz. By fitting a simulation curve to the experimental data, as seen in Figure 3c, we extrapolated a 3 dB bandwidth of 5.66 MHz. This modulation speed has a few MHz dependence on the detuning, but this finding indicates that the acoustic resonance tuning

https://doi.org/10.1021/acs.nanolett.4c00335
Nano Lett. 2024, 24, 7143−7149

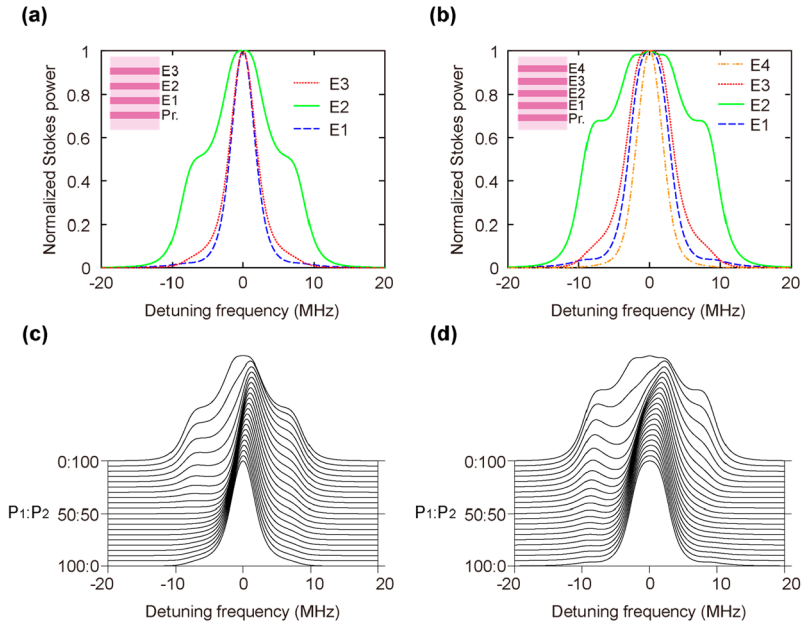

Figure 5. Bandwidth and frequency tuning with higher-order Lorentzian responses. Normalized Stokes output spectra for (a) four- and (b) five-coupled acoustic cavities are shown. The index E1 represents the channel nearest to the probe, with higher indices indicating channels further from the probe, as seen in the insets of (a) and (b). Blue dashed lines correspond to E1, green solid lines correspond to E2, red dotted lines correspond to E3, and black dash-dotted lines correspond to E4. Normalized Stokes output spectra with different pump power ratios, P_1:P_2 values for (c) four-coupled and (d) five-coupled acoustic cavities are also presented. The relative phase of the two pumps is fixed at π.

can alternate between narrow- and wide-bandwidth operations at speeds of around 5 MHz.

In addition, we measured the peak frequency tunability of the device. Our system has high-order Lorentzian responses, so we focus on the peak frequency, which has the maximum value on the frequency response, rather than the center frequency of the Lorentzian function since this point has the maximum signal-to-noise ratio. Spectra are obtained by varying the power ratio between S_1 and S_2 while keeping the sum of S_1 and S_2 constant, as shown in Figure 4. Due to different Brillouin gain coefficients on the pump channels, we redefine $S_1 = g_1\Gamma_0/2 \times P_1$ and $S_2 = g_2 J \times P_2$, where g_1 and g_2 represent the strengths of Brillouin interaction in channels 1 and 2, respectively. In the experiment, we measure a dip in the output spectrum at a 5:5 ratio and $\phi = -\pi/2$, as shown in Figure 4c. The dip occurs when the contribution to the acoustic field on the probe channel from channel 1 is destructively interfered with that from channel 2, as in eq 1. The dip measurement confirms the power balance between S_1 and S_2. Subsequently, we alter the ratio of S_1 and S_2 while maintaining their constant sum.

Figure 4a−e shows peak-frequency-shifted spectra for various pump ratios, with relative phases ϕ between S_1 and S_2 set at 0, π, and $-\pi/2$. The spectra are normalized to the peak value of Figure 4a. Due to the nonidentical nature of the acoustic cavities, the right-shifted peaks ($\phi = 0$) are smaller than the left-shifted peaks ($\phi = \pi$) by 2 dB. The results show that when the power ratios are 3:7, 5:5, and 7:3, the peak frequency shifts with relative phase $[\pi, 0]$ are $[-0.6, 1]$, $[-1, 1.75]$, and $[-0.8, 1.2]$ MHz, respectively. A maximum peak frequency shift of 2.75 MHz is achieved, corresponding to 53% of an average dissipation rate of 5.13 MHz. Furthermore, the 2.75 MHz tuning range exceeds the resonant frequency deviations caused by fabrication errors in our system. While the peak frequency is varied, the corresponding peak power level varies by less than 2 dB. Figure 4f,g shows the collections of fitting envelopes for $\phi = 0$ and π, respectively. The tunings of the peak frequency and bandwidth are clearly observed, as illustrated in Figure 1c,d, which represent ideal cases.

Greater tunability can be achieved by incorporating higher-order Lorentzian responses. As shown in Figure 5a,b, the bandwidth tunability of the multiport device is calculated for four- and five-coupled acoustic cavities, respectively. With a dissipation rate of 5 MHz, the acoustic resonant responses are calculated by extending the three-acoustic-cavity system model. The coupling strengths (J_i) between the cavities are numerically determined using differential evolution and Nelder−Mead algorithms to optimize the bandwidth tunability without splitting the resonant response peak.[44] For four-coupled acoustic cavities, when exciting E1, E2, and E3 individually, coupling strengths of $[J_3, J_2, J_1] = [6.89, 4.17, 1.28]$ MHz are obtained, yielding bandwidths of 3.90, 13.41, and 4.29 MHz, respectively, as seen in Figure 5a. For five-coupled acoustic cavities, exciting E1, E2, E3, and E4 individually, optimized coupling strengths of $[J_4, J_3, J_2,$ and $J_1] = [1.34, 7.49, 4.66,$ and $2.50]$ MHz are achieved, with bandwidths of 6.12, 18.46, 7.19, and 4.28 MHz, respectively, as shown in Figure 5b. Figure 5c,d shows greater frequency tunability in four- and five-coupled acoustic cavities. In these figures, high-order Lorentzian responses excited from E1:E2 in four-coupled and five-coupled cavities are coherently mixed with a relative phase of π, respectively. We also observe that the peak frequency is shifted in the negative direction when the relative phase is zero. The maximum peak shifts are about ± 2.55 MHz ($0.51\Gamma_0$, four-coupled cavities) and ± 4.46 MHz ($0.892\Gamma_0$, five-coupled cavities). These results clearly indicate that the tunable range can be significantly enhanced with multiple acoustic cavities, and the engineering of output spectra is highly feasible since the relative phases and power ratios of oscillating input pump lasers can be easily controlled.

https://doi.org/10.1021/acs.nanolett.4c00335
Nano Lett. 2024, 24, 7143−7149

In this paper, we demonstrate a novel method of acoustic resonance tuning by mixing high-order Lorentzian responses. Here, our active tuning is achieved without controls of mechanical parameters but with redistribution of mechanical modes (mixing of high-order Lorentzian responses). The mode redistribution may alter the response of mechanical oscillators, for instance, efficiencies and bandwidths. We can minimize such alternations by designing coupling strengths through phononic crystals. In our device, the weakly coupled scheme reduces the effect of energy redistribution on the probe channel during the changes in power ratios, so the efficiency changes by less than 2 dB. Also, the bandwidths are almost unchanged while the frequency shifting is maximized (Figure S4c–e in the Supporting Information). Therefore, proper device designs are required to achieve stable operations with energy redistribution between acoustic supermodes.

In summary, we have demonstrated for the first time an optically tunable acoustic resonance based on high-order Lorentzian mixing. Active control of acoustic resonators is typically challenging without piezoelectricity or large thermal effects. Here, our device is capable of adjusting its bandwidth and peak frequency simply by coherently mixing two Lorentzian responses in silicon without piezoelectricity and with a small thermal expansion coefficient.[45] This approach paves the way for innovative tuning methods in complementary metal-oxide-semiconductor (CMOS) compatible mechanical devices and optomechanics.

■ ASSOCIATED CONTENT

Supporting Information

The Supporting Information is available free of charge at https://pubs.acs.org/doi/10.1021/acs.nanolett.4c00335.

Details of fabrication methods, experimental method, theoretical models, and example of signal processing application (PDF)

■ AUTHOR INFORMATION

Corresponding Author

Heedeuk Shin − *Department of Physics, Pohang University of Science and Technology (POSTECH), Pohang 37673, Republic of Korea;* orcid.org/0000-0002-6846-3971; Email: heedeukshin@postech.ac.kr

Authors

Hyeongpin Kim − *Department of Physics, Pohang University of Science and Technology (POSTECH), Pohang 37673, Republic of Korea;* Present Address: Samsung Electronics, 34 Samsungjeonja-ro, Hwaseong 18450, Republic of Korea

Yeolheon Seong − *Department of Physics, Pohang University of Science and Technology (POSTECH), Pohang 37673, Republic of Korea*

Kiwon Kwon − *Department of Physics, Pohang University of Science and Technology (POSTECH), Pohang 37673, Republic of Korea*

Taek Yong Hwang − *Molding and Metal Forming R&D Department, Korea Institute of Industrial Technology, Bucheon 14441, Republic of Korea;* orcid.org/0000-0003-0402-8361

Complete contact information is available at: https://pubs.acs.org/10.1021/acs.nanolett.4c00335

Author Contributions

H.K. conceived the idea. H.K., Y.S., and K.K. fabricated the devices. H.K. and Y.S. designed and carried out the experiments. H.K. performed the theoretical study and data analysis with help of T.Y.H. H.S. supervised the project. H.K. and H.S. wrote the manuscript with contributions from all authors.

Notes

The authors declare no competing financial interest.

■ ACKNOWLEDGMENTS

We thank Kyong-Tae Park for helpful discussions. We also thank Korea Advanced Nano Fab Center (KANC) for technical support in device fabrications. This work was supported by the Institute for Information & communications Technology Promotion (IITP) (2020-0-00947, IITP-2023-RS-2023-00227854) and the MSIT (Ministry of Science and ICT), Korea, under the ITRC (Information Technology Research Center) support program (IITP-2022-RS-2022-00164799) supervised by the IITP.

■ REFERENCES

(1) Dinh, T.; Rais-Zadeh, M.; Nguyen, T.; Phan, H. P.; Song, P.; Deo, R.; Dao, D.; Nguyen, N. T.; Bell, J. Micromachined Mechanical Resonant Sensors: From Materials, Structural Designs to Applications. *Adv. Mater. Technol.* **2024**, *9*, 2300913.

(2) Aspelmeyer, M.; Kippenberg, T. J.; Marquardt, F. Cavity Optomechanics. *Rev. Mod. Phys.* **2014**, *86*, 1391.

(3) Maccabe, G. S.; Ren, H.; Luo, J.; Cohen, J. D.; Zhou, H.; Sipahigil, A.; Mirhosseini, M.; Painter, O. Nano-Acoustic Resonator with Ultralong Phonon Lifetime. *Science* **2020**, *370*, 840–843.

(4) Safavi-Naeini, A. H.; Van Thourhout, D.; Baets, R.; Van Laer, R. Controlling Phonons and Photons at the Wavelength Scale: Integrated Photonics Meets Integrated Phononics. *Optica* **2019**, *6*, 213–232.

(5) Shnaiderman, R.; Wissmeyer, G.; Ülgen, O.; Mustafa, Q.; Chmyrov, A.; Ntziachristos, V. A Submicrometre Silicon-on-Insulator Resonator for Ultrasound Detection. *Nature* **2020**, *585*, 372–378.

(6) Westerveld, W. J.; Mahmud-Ul-Hasan, M.; Shnaiderman, R.; Ntziachristos, V.; Rottenberg, X.; Severi, S.; Rochus, V. Sensitive, Small, Broadband and Scalable Optomechanical Ultrasound Sensor in Silicon Photonics. *Nat. Photonics* **2021**, *15*, 341–345.

(7) Schliesser, A.; Arcizet, O.; Rivière, R.; Anetsberger, G.; Kippenberg, T. J. Resolved-Sideband Cooling and Position Measurement of a Micromechanical Oscillator Close to the Heisenberg Uncertainty Limit. *Nat. Phys.* **2009**, *5*, 509–514.

(8) Wu, M.; Wu, N. L. Y.; Firdous, T.; Fani Sani, F.; Losby, J. E.; Freeman, M. R.; Barclay, P. E. Nanocavity Optomechanical Torque Magnetometry and Radiofrequency Susceptometry. *Nat. Nanotechnol* **2017**, *12*, 127–131.

(9) Wu, M.; Hryciw, A. C.; Healey, C.; Lake, D. P.; Jayakumar, H.; Freeman, M. R.; Davis, J. P.; Barclay, P. E. Dissipative and Dispersive Optomechanics in a Nanocavity Torque Sensor. *Phys. Rev. X* **2014**, *4*, No. 021052.

(10) Blaikie, A.; Miller, D.; Alemán, B. J. A Fast and Sensitive Room-Temperature Graphene Nanomechanical Bolometer. *Nat. Commun.* **2019**, *10*, 4726.

(11) Chen, Y.; Liu, S.; Hong, G.; Zou, M.; Liu, B.; Luo, J.; Wang, Y. Nano-Optomechanical Resonators for Sensitive Pressure Sensing. *ACS Appl. Mater. Interfaces* **2022**, *14*, 39211–39219.

(12) Gil-Santos, E.; Ramos, D.; Martínez, J.; Fernández-Regúlez, M.; García, R.; San Paulo, Á.; Calleja, M.; Tamayo, J. Nanomechanical Mass Sensing and Stiffness Spectrometry Based on Two-Dimensional Vibrations of Resonant Nanowires. *Nat. Nanotechnol* **2010**, *5*, 641–645.

(13) Marpaung, D.; Roeloffzen, C.; Heideman, R.; Leinse, A.; Sales, S.; Capmany, J. Integrated Microwave Photonics. *Laser Photon Rev.* **2013**, *7*, 506−538.
(14) Li, J.; Lee, H.; Vahala, K. J. Microwave Synthesizer Using an On-Chip Brillouin Oscillator. *Nat. Commun.* **2013**, *4*, 2097.
(15) Merklein, M.; Stiller, B.; Vu, K.; Madden, S. J.; Eggleton, B. J. A Chip-Integrated Coherent Photonic-Phononic Memory. *Nat. Commun.* **2017**, *8*, 574.
(16) Shin, H.; Cox, J. A.; Jarecki, R.; Starbuck, A.; Wang, Z.; Rakich, P. T. Control of Coherent Information via on Chip Photonic-Phononic Emitter-Receivers. *Nat. Commun.* **2015**, *6*, 6427.
(17) Kim, H.; Seong, Y.; Kwon, K.; Shin, W.; Lee, S.; Shin, H. On-Chip RF Signal Shaping by Coherent Control of Optically Driven Acoustic Wave Interference. *ACS Photonics* **2022**, *9*, 2938−2945.
(18) Kim, H.; Shin, H. Active Information Manipulation via Optically Driven Acoustic-Wave Interference. *Nano Lett.* **2021**, *21*, 7270−7276.
(19) Choudhary, A.; Liu, Y.; Marpaung, D.; Eggleton, B. J. On-Chip Brillouin Filtering of RF and Optical Signals. *IEEE J. Sel. Top. Quantum Electron.* **2018**, *24*, 1.
(20) Marpaung, D.; Morrison, B.; Pagani, M.; Pant, R.; Choi, D.-Y.; Luther-Davies, B.; Madden, S. J.; Eggleton, B. J. Low-Power, Chip-Based Stimulated Brillouin Scattering Microwave Photonic Filter with Ultrahigh Selectivity. *Optica* **2015**, *2*, 76−83.
(21) Pagani, M.; Marpaung, D.; Choi, D. Y.; Madden, S. J.; Luther-Davies, B.; Eggleton, B. J. Tunable Microwave Photonic Phase Shifter Using On-Chip Stimulated Brillouin Scattering. *Opt Express* **2014**, *22*, 28810−28818.
(22) Merklein, M.; Stiller, B.; Eggleton, B. J. Brillouin-Based Light Storage and Delay Techniques. *Journal of Optics* **2018**, *20*, No. 083003.
(23) Eggleton, B. J.; Poulton, C. G.; Rakich, P. T.; Steel, M. J.; Bahl, G. Brillouin Integrated Photonics. *Nat. Photonics* **2019**, *13*, 664−677.
(24) Stiller, B.; Merklein, M.; Wolff, C.; Vu, K.; Ma, P.; Madden, S. J.; Eggleton, B. J. Coherently Refreshing Hypersonic Phonons for Light Storage. *Optica* **2020**, *7*, 492−497.
(25) McKay, L.; Merklein, M.; Casas Bedoya, A.; Choudhary, A.; Jenkins, M.; Middleton, C.; Cramer, A.; Devenport, J.; Klee, A.; Desalvo, R.; Eggleton, B. J. Brillouin-Based Phase Shifter in a Silicon Waveguide. *Optica* **2019**, *6*, 907−913.
(26) McKay, L.; Merklein, M.; Choudhary, A.; Liu, Y.; Jenkins, M.; Middleton, C.; Cramer, A.; Chilton, A.; Devenport, J.; Vu, K.; Choi, D. Y.; Ma, P.; Madden, S. J.; Desalvo, R.; Eggleton, B. J. Broadband Brillouin Phase Shifter Utilizing RF Interference: Experimental Demonstration and Theoretical Analysis. *Journal of Lightwave Technology* **2020**, *38*, 3624−3636.
(27) Mirhosseini, M.; Sipahigil, A.; Kalaee, M.; Painter, O. Superconducting Qubit to Optical Photon Transduction. *Nature* **2020**, *588*, 599−603.
(28) Safavi-Naeini, A. H.; Gröblacher, S.; Hill, J. T.; Chan, J.; Aspelmeyer, M.; Painter, O. Squeezed Light from a Silicon Micromechanical Resonator. *Nature* **2013**, *500*, 185−189.
(29) Safavi-Naeini, A. H.; Chan, J.; Hill, J. T.; Alegre, T. P. M.; Krause, A.; Painter, O. Observation of Quantum Motion of a Nanomechanical Resonator. *Phys. Rev. Lett.* **2012**, *108*, No. 033602.
(30) Cohen, J. D.; Meenehan, S. M.; MacCabe, G. S.; Gröblacher, S.; Safavi-Naeini, A. H.; Marsili, F.; Shaw, M. D.; Painter, O. Phonon Counting and Intensity Interferometry of a Nanomechanical Resonator. *Nature* **2015**, *520*, 522−525.
(31) Bagci, T.; Simonsen, A.; Schmid, S.; Villanueva, L. G.; Zeuthen, E.; Appel, J.; Taylor, J. M.; Sørensen, A.; Usami, K.; Schliesser, A.; Polzik, E. S. Optical Detection of Radio Waves through a Nanomechanical Transducer. *Nature* **2014**, *507*, 81−85.
(32) Hsu, W. T.; Brown, A. R. Frequency Trimming for MEMS Resonator Oscillators. *IEEE International Frequency Control Symposium Joint with the 21st European Frequency and Time Forum*; 2007; pp 1088−1091.
(33) Hatipoglu, U.; Sonar, S.; Lake, D. P.; Meesala, S.; Painter, O. In-Situ Tuning of Optomechanical Crystals with Nano-Oxidation. *Optica* **2024**, *11*, 371−375.
(34) De Laat, M. L. C.; Pérez Garza, H. H.; Herder, J. L.; Ghatkesar, M. K. A Review on in Situ Stiffness Adjustment Methods in MEMS. *Journal of Micromechanics and Microengineering* **2016**, *26*, No. 063001.
(35) Shao, L.; Zhu, D.; Colangelo, M.; Lee, D.; Sinclair, N.; Hu, Y.; Rakich, P. T.; Lai, K.; Berggren, K. K.; Lončar, M. Electrical Control of Surface Acoustic Waves. *Nat. Electron* **2022**, *5*, 348−355.
(36) Karabalin, R. B.; Villanueva, L. G.; Matheny, M. H.; Sader, J. E.; Roukes, M. L. Stress-Induced Variations in the Stiffness of Micro-and Nano-Cantilever Beams. *Phys. Rev. Lett.* **2012**, *108*, 236101.
(37) Ye, F.; Lee, J.; Feng, P. X. L. Electrothermally Tunable Graphene Resonators Operating at Very High Temperature up to 1200 K. *Nano Lett.* **2018**, *18*, 1678−1685.
(38) Barton, R. A.; Storch, I. R.; Adiga, V. P.; Sakakibara, R.; Cipriany, B. R.; Ilic, B.; Wang, S. P.; Ong, P.; McEuen, P. L.; Parpia, J. M.; Craighead, H. G. Photothermal Self-Oscillation and Laser Cooling of Graphene Optomechanical Systems. *Nano Lett.* **2012**, *12*, 4681−4686.
(39) Hatanaka, D.; Mahboob, I.; Onomitsu, K.; Yamaguchi, H. Phonon Waveguides for Electromechanical Circuits. *Nat. Nanotechnol* **2014**, *9*, 520−524.
(40) Mayor, F. M.; Jiang, W.; Sarabalis, C. J.; McKenna, T. P.; Witmer, J. D.; Safavi-Naeini, A. H. Gigahertz Phononic Integrated Circuits on Thin-Film Lithium Niobate on Sapphire. *Phys. Rev. Appl.* **2021**, *15*, No. 014039.
(41) Peng, M.; Cheng, J.; Zheng, X.; Ma, J.; Feng, Z.; Sun, X. 2D-Materials-Integrated Optoelectromechanics: Recent Progress and Future Perspectives. *Rep. Prog. Phys.* **2023**, *86*, No. 026402.
(42) Kittlaus, E. A.; Shin, H.; Rakich, P. T. Large Brillouin Amplification in Silicon. *Nat. Photonics* **2016**, *10*, 463−468.
(43) Shin, H.; Qiu, W.; Jarecki, R.; Cox, J. A.; Olsson, R. H.; Starbuck, A.; Wang, Z.; Rakich, P. T. Tailorable Stimulated Brillouin Scattering in Nanoscale Silicon Waveguides. *Nat. Commun.* **2013**, *4*, 1944.
(44) Gao, F.; Han, L. Implementing the Nelder-Mead Simplex Algorithm with Adaptive Parameters. *Comput. Optim Appl.* **2012**, *51*, 259−277.
(45) Middelmann, T.; Walkov, A.; Bartl, G.; Schödel, R. Thermal Expansion Coefficient of Single-Crystal Silicon from 7 to 293 K. *Phys. Rev. B* **2015**, *92*, 174113.

https://doi.org/10.1021/acs.nanolett.4c00335
Nano Lett. 2024, 24, 7143−7149